

# Nanostructure Evolution: From Aggregated to Spherical SiO<sub>2</sub> Particles Made in Diffusion Flames

Adrian Camenzind,<sup>[a]</sup> Heiko Schulz,<sup>[a]</sup> Alexandra Teleki,<sup>[a]</sup> Gregory Beaucage,<sup>[b]</sup> Theyencheri Narayanan,<sup>[c]</sup> and Sotiris E. Pratsinis\*<sup>[a]</sup>

**Keywords:** Nanoparticles / Silica / Diffusion flame / SAXS

The formation of nanostructured silica particles by oxidation of hexamethyldisiloxane (HMDSO) in co-annular diffusion flames is investigated by *in-situ* small-angle X-ray scattering (SAXS). This enabled the nonintrusive monitoring of the mass fractal dimension, the aggregate size, and the number of primary particles per aggregate, along with the silica volume fraction, the primary particle diameter, the geometric standard deviation, and the number density along the flame axis. Parallel to this, thermophoretic sampling (TS) of the particles and analysis by transmission electron microscopy (TEM) allowed for direct comparison of particle morphology to that obtained from the above SAXS analysis, which were compared also to the ultra-small-angle X-ray scattering (US-

AXS) data for product particles collected from the filter. The flame temperature was measured by *in-situ* Fourier transform infrared (FTIR) spectroscopy. By increasing the oxygen flow rate, the laminar diffusion flame changed to a turbulent, premixed-like flame. Non-aggregated, spherical particles were formed in the former, while aggregates were formed in the latter flame. The relatively long high-temperature particle residence times in the laminar diffusion flame facilitated sintering of the aggregates formed earlier into compact spherical particles at later stages of the flame.

(© Wiley-VCH Verlag GmbH & Co. KGaA, 69451 Weinheim, Germany, 2008)

## Introduction

Flame aerosol synthesis of ceramic nanoparticles is attractive as it does not require the multiple steps of wet chemistry and the cleaning of liquid by-products, which results in high-purity products (e.g. optical fibers), while particle collection is easier from gas than liquid streams.<sup>[1]</sup> As a result, this aerosol route is preferred in the manufacture of materials (pigmentary TiO<sub>2</sub> by the “chloride” versus the “sulfate” process) or in the cleaning of process streams (gas vs. wet scrubbing). For example, while some years ago flame synthesis of pigmentary titania covered a fraction of the world's production, it now provides 60 % of the world's production with a \$5 billion value.<sup>[2]</sup> So within 20 years the “chloride” process is expected to dominate this field. Today flame aerosol technology is used in the large-scale manufacture of carbon black, fumed SiO<sub>2</sub>, TiO<sub>2</sub>, Al<sub>2</sub>O<sub>3</sub>, and even UO<sub>2</sub> nanoparticles with a rate of several tons/hour.<sup>[2,3]</sup> Furthermore, it is dominant in the manufacture of light-

guide preforms for telecommunications and is used in direct particle synthesis and deposition.

Most of this industrial development took place by valiant evolutionary research with the exception of the optical fiber industry.<sup>[4]</sup> In the last 10–20 years, however, research at academic and industrial laboratories has contributed to a better understanding of this technology. Pioneer work in this field was done by Ulrich,<sup>[3]</sup> while detailed reviews were written by Pratsinis,<sup>[4]</sup> Wooldridge,<sup>[5]</sup> Kammler et al.,<sup>[6]</sup> and, most recently, by Roth.<sup>[7]</sup> Process control issues were addressed by Christofides et al.<sup>[8]</sup> Very recently, an array of sophisticated products such as catalysts,<sup>[9]</sup> sensors, dental and bone replacement composites, phosphors, fuel cell and battery materials, and even nutritional supplements have been made in flames.<sup>[10]</sup>

Today, there is a reasonably good understanding for the control of flame-made particle sizes, polydispersity, and crystallinity, but to a lesser extent morphology. For example, by controlling precursor concentration and the high-temperature particle residence time, it is possible to predict the evolution of TiO<sub>2</sub> particle size made in premixed flame reactors from first principles.<sup>[11]</sup> From an operational point of view, this understanding means, for example, that by increasing the oxidant flow rate, the primary SiO<sub>2</sub> particle size decreases, while by increasing its precursor flow rate, the SiO<sub>2</sub> particle size increases.<sup>[12]</sup> Flame-made particles are more polydisperse than wet-made ones, as the former rapidly attain the self-preserving distribution by coagula-

[a] Particle Technology Laboratory, Institute of Process Engineering, Department of Mechanical and Process Engineering, ETH Zurich,

Sonneggstrasse 3, 8092 Zurich, Switzerland

Fax: +41-44-632-15-95

E-mail: pratsinis@ptl.mavt.ethz.ch

[b] Department of Chemical and Materials Engineering, University of Cincinnati,

Cincinnati, Ohio 45221-0012, USA

[c] European Synchrotron Radiation Facility (ESRF), 38043 Grenoble, France

tion.<sup>[4]</sup> Within an aggregate, however, primary particles tend to be quite monodisperse by sintering<sup>[13]</sup> so they exhibit a performance that is typically attributed to quantum dots (e.g. for ZnO<sup>[14]</sup>).

With respect to crystallinity, again high-temperature residence time, particle size, and gas composition determine the crystal-phase composition, following thermodynamics. This is, however, more challenging in flames as the short residence times place kinetic constraints in the rapid development of desirable product phases. Nevertheless, this contributes to the synthesis of metastable phases and new materials with unprecedented performance.<sup>[15]</sup> In industrial practice, desired phases are selected typically by additives. For example, in the manufacture of TiO<sub>2</sub> pigments, the rutile phase in the product is assured by doping with aluminum.<sup>[16]</sup>

Contrary to particle size and crystallinity, control of product morphology remains one of the most challenging characteristics of flame-made particles, as there are no standardized diagnostics for it. At the same time, nanoparticle morphology is of prime practical interest. Ideally, non-aggregated, single, spherical particles are required for nano composites in optical materials (e.g. paint slurries or dental prosthetics) and as wafer-processing agents (chemical-mechanical polishing) in the microelectronic industry.<sup>[17]</sup> Aggregated (chemically bonded or bonded by sintering) or agglomerated (physically bonded) primary particles are attractive as catalysts,<sup>[9]</sup> as reinforcing in composites<sup>[6]</sup> (e.g. tires), for the deposition on optical fiber preforms, which facilitates water and chlorine removal from the preform prior to fiber drawing. As a result, there is considerable interest in controlling particle structure, as it is not easy to change it by post-processing.<sup>[4]</sup>

The goal of this paper is to advance the current understanding of fumed SiO<sub>2</sub> structure development in diffusion flame reactors. Silica nanoparticles are selected as they are the standard additive for enhancing the rheology of suspensions. Diffusion flame reactors are selected here because of their flexibility in the safe synthesis of particulate products (e.g. heterogeneous catalysts,<sup>[9,10]</sup> photocatalysts<sup>[9,18]</sup> and precursors to carbides<sup>[19,20]</sup>) with a wide spectrum of sizes and crystallinities within their process parameter space. Here, the evolution of the structure is monitored by SAXS, which non-intrusively traces the evolution of primary particle and aggregate sizes, polydispersity, and fractal dimension of powders made in uniform premixed<sup>[21]</sup> and diffusion flame reactors.<sup>[22]</sup> The SAXS data are consistent with particle images collected by thermophoretic sampling along the path of particle formation.<sup>[21]</sup> The SAXS method distinguishes *ex-situ* aggregated TiO<sub>2</sub> particles from agglomerated particles made in diffusion flames<sup>[23]</sup> and was already used to trace the evolution of particle structure in such reactors.<sup>[21,22]</sup> Here, SiO<sub>2</sub> particles are made in a diffusion flame reactor, which leads to either aggregated or spherical particles.<sup>[12]</sup> The development of either one of these structures is monitored in detail (primary and aggregate particle size, fractal dimension, polydispersity, number of primary particles per aggregate) by SAXS, as well as by microscopy

along the flame axis, and is correlated to the flame temperature determined by *in-situ* Fourier transform infrared spectroscopy (FTIR).<sup>[24]</sup>

## Results and Discussion

Figure 1 shows TEM images of silica formed at a rate of 4.8 g/h in diffusion flames at four O<sub>2</sub> flow rates ranging from 2 to 10 L/min (*S*-2 to *S*-10). The average particle size decreases with increasing O<sub>2</sub> flow rate, which is consistent with the literature.<sup>[2,12,25]</sup> The particles formed at a low O<sub>2</sub> flow rate (*S*-2) appear spherical and non-aggregated. Those formed at a high O<sub>2</sub> flow rate (*S*-10) are highly aggregated,<sup>[12]</sup> even though some spherical particles are present (Figure 1, *S*-7 and *S*-10), which arise from the broad residence time distribution of the particles collected on the filter. The fraction of such spheres decreases (from *S*-7 to *S*-10) with increasing  $\Delta v$  ( $v$  is the velocity), that increases turbulence and mixing, which leads to uniform particle morphology (e.g. see Figure 8 in ref.<sup>[2]</sup>). Figure 1 shows also the BET equivalent particle size ( $d_{\text{BET}}$ ) of these particles (diamonds) as a function of the relative gas exit velocities of the precursor (fuel) and O<sub>2</sub> streams ( $\Delta v = v_{\text{O}_2} - v_{\text{fuel}}$ ). The present data are consistent with the diffusion flame operation line for SiO<sub>2</sub> formed at 5 g/h (solid line).<sup>[2]</sup> According to that analysis, even though a diffusion flame is employed, the  $d_{\text{BET}}$  at high oxygen flow rates (Figure 1: *S*-7 and *S*-10) is insensitive to increasing  $\Delta v$  values. This indicates that practically a turbulent, premixed-like flame was formed under these conditions even though a diffusion flame is used.<sup>[2]</sup> As a result, only the results from the two extreme conditions *S*-2 and *S*-10 will be discussed below; the flames under these conditions are therefore referred to as the “laminar” (*S*-2) and the “turbulent” diffusion flame (*S*-10).

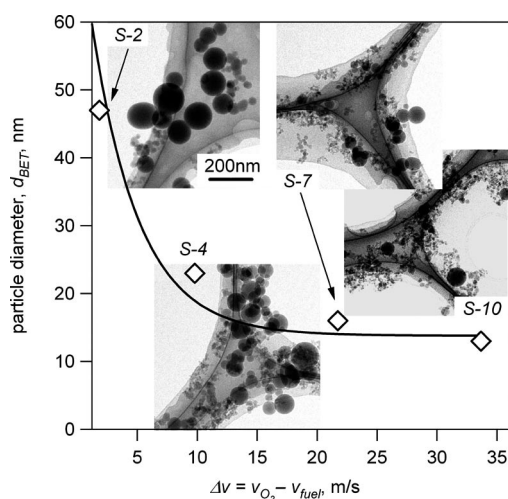


Figure 1. BET-equivalent SiO<sub>2</sub> particle diameter (symbols) from diffusion flames *S*-*y* (where *y* is the supplied O<sub>2</sub> flow rate in L/min) as a function of velocity difference of oxygen from fuel gas at the burner face along with the operation line of a diffusion flame producing 5 g/h silica<sup>[2]</sup> and TEM images of the corresponding particles collected from the filter (same scale bar for all images).

Figure 2 shows the scattering intensities of particles from both *ex-situ* USAXS (a: particle product from *S-10*) and *in-situ* SAXS (b: *S-2* at different heights above burner, HAB) as a function of scattering vector,  $q$ . Figure 2a shows that at high  $q$  ( $0.02 < q < 0.05$ ), the power law (Porod's law)<sup>[26,27]</sup> decay has a slope equal to  $-4$ , which indicates a smooth particle surface (*PI*). Towards lower  $q$  values, first a knee-like decay (Guinier's law, *G1*)<sup>[26,27]</sup> depicted by  $q \propto 1/R_{g1}$  follows, which is proportional to the reciprocal of the scattering size (equivalent to the primary particle size). The second Porod regime (*P2*:  $0.001 < q < 0.01$ ) depicts the mass fractal dimension (here  $D_f = 1.64$ )<sup>[26,27]</sup> and above that, in the second Guinier regime, the characteristic larger size structure, the aggregate size ( $R_{g2}$  or simply here  $R_g = 130$  nm), is depicted.

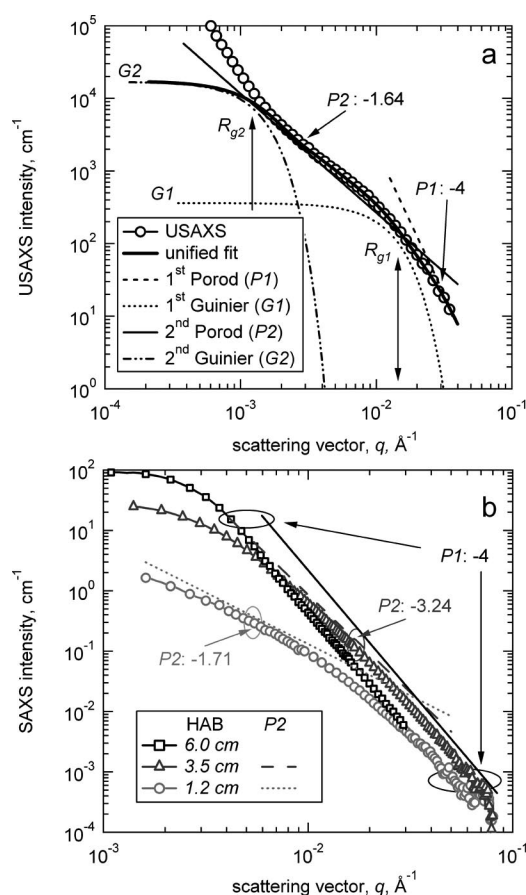


Figure 2. Scattering intensities as a function of scattering vector  $q$ : (a) *ex-situ* USAXS of particles (*S-10*) collected from the filter and the unified fit (bold solid line) along two Guinier (*G1*, *G2*) and Porod (*P1*, *P2*) regimes, showing  $D_f$  of 1.64, a smooth primary particle surface (slope of  $-4$ ) and two characteristic sizes,  $R_{g2}$  and  $R_{g1}$ , which correspond to aggregate and primary particle sizes; (b) *in-situ* SAXS of particles of the *S-2* flame at HAB = 1.2, 3.5, and 6 cm. Slopes of the second Porod regime (*P2*) depicting a fractal dimension increase from  $D_f = 1.71$  (mass fractal, HAB = 1.2 cm) to  $D_f = 2.76$  (surface fractal, HAB = 3.5). Two slopes can be distinguished, which correspond to the two sizes of the aggregates. At HAB = 6 cm, large primary particles having a smooth surface (slope of  $-4$ ) are formed. A single slope is obtained, which is indicative of non-aggregated particles as they can be described by a single size.<sup>[23]</sup>

In Figure 2b *in-situ* SAXS data of particles at HAB = 1.2, 3.5, and 6.0 cm in the *S-2* flame are shown. All scattering intensities decay in the first Porod regime (*P1*:  $0.04 < q < 0.07$ ) with a slope of  $-4$  (smooth particle surface). The knee-like decay (Guinier regime, *G1*) at HAB = 1.2 and 3.5 cm starts at higher  $q$  values, which means smaller primary particles ( $d_{v/s} = 9\text{--}14$  nm) than those at HAB = 6.0, whereas the Porod regime (*P1*) extends to lower  $q$  values ( $0.004 < q < 0.03$ ) and also shifts the first Guinier regime (*G1*) to low  $q$  values, hence large primary particles are obtained ( $d_{v/s} = 90$  nm). The second Porod regime (*P2*) at low HAB values (1.2 and 3.5 cm) shows fractal-like structures, with slopes of  $-1.71$  and  $-3.24$ , respectively. The fractal structure of the latter particles can no longer be described with the conventional mass fractal theory, as the power law decline in the second regime is steeper than  $-3$ , which means that  $D_f$  should be larger than 3 or the particles are no longer fractal-like.<sup>[28]</sup> The dense structure of these aggregates can be interpreted as compact, non-fractal-like particles having a surface roughness evoked by the small primary particles. Here, the surface fractal dimension was used to describe the surface texture.<sup>[28]</sup>

Figure 3 shows the temperature (filled symbols) along the axis of the laminar *S-2* (triangles) and turbulent *S-10* (circles) flames. The maximum temperature ( $\approx 2500$  K) of the laminar flame occurs at HAB = 0.5–3.5 cm, which coincides with the (yellowish) flame reaction zone where reactants mix and react. It should be noted that this apparent isothermal region is an average across the flame. In fact, at a position low in the diffusion flame center axis, the temperature is well below the radial average measured by FTIR spectroscopy as the flame front is positioned off the flame axis.<sup>[29]</sup> At the visual end of the flame (HAB = 7.5 cm, Table 1), the temperature is 1900 K.

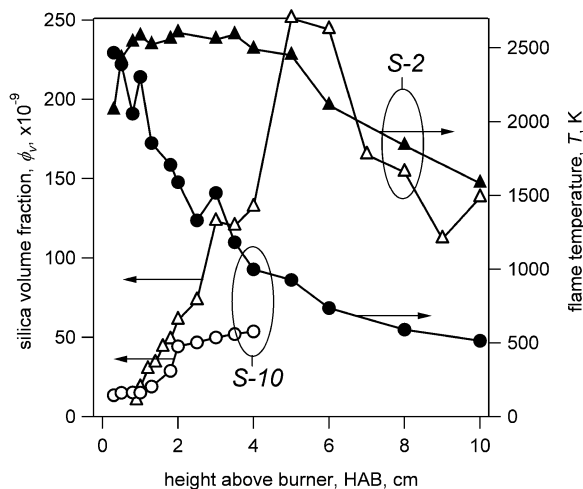


Figure 3. Flame temperature  $T$  (filled symbols) determined from FTIR spectroscopy and silica volume fraction  $f_v$  (open symbols) determined from SAXS as a function of HAB for the laminar (*S-2*, triangles) and turbulent flames (*S-10*, circles).

In the turbulent flame (*S-10*), fast mixing of reactants<sup>[2]</sup> results in an initially high temperature (Figure 3 at HAB = 0.5 cm) similar to that of the *S-2* flame, but decreases to

Table 1. Gas flow rates, flame height, and product particle sizes (determined by BET and USAXS) for the diffusion flames producing SiO<sub>2</sub> (*S-y*) and background flames used as baseline in SAXS (no particle production) are given in brackets (*B-y*) – *y* is the flow rate of oxygen [L/min].

Flame – O <sub>2</sub> flow	CH <sub>4</sub> [L/min]	Total flow [L/min]	Flame height [cm]	$d_{\text{BET}}$ [nm]	$d_{\text{v/s}}$ [nm]
<i>S-2 (B-2)</i>	0.5 (0.6)	3.3 (3.4)	7.5 (7.0)	47	48
<i>S-4 (B-4)</i>	0.5 (0.6)	5.3 (5.4)	6.0 (4.0)	23	35
<i>S-7 (B-7)</i>	0.5 (0.6)	8.3 (8.4)	4.0 (3.0)	16	14
<i>S-10 (B-10)</i>	0.5 (0.6)	11.3 (11.4)	3.5 (2.5)	13	11

1000 K towards the visual flame end (HAB = 3.5 cm, Table 1). The higher cooling rate of the *S-10* flame than the *S-2* flame is attributed to the turbulence-induced mixing of excess O<sub>2</sub> and air entrainment, which rapidly cools the flame.<sup>[30]</sup>

Figure 3 also shows that the SiO<sub>2</sub> volume fraction ( $\phi_v$ , open symbols) in the *S-2* flame (triangles) increases with HAB and approaches a maximum towards the end of the (yellow) flame reaction zone (HAB < 3 cm), where most of the fuel and precursor are consumed according to FTIR spectroscopy (not shown here).<sup>[12]</sup> Further downstream (HAB > 6 cm), air entrainment diluted the particle-laden gas stream, which lowers  $\phi_v$ .<sup>[21]</sup> The value of  $\phi_v$  in the turbulent flame (*S-10*, open circles) reaches a maximum at HAB = 3–4 cm, which coincides with the visual flame length (Table 1). This maximum  $\phi_v$ ,  $5 \times 10^{-8}$ , is about five times smaller than that of the *S-2* flame ( $2.5 \times 10^{-7}$ ), which corresponds roughly to the five-times higher O<sub>2</sub> flow rate and stronger air entrainment by turbulence in the *S-10* flame than that of the *S-2* flame. At low HAB (< 1 cm), higher  $\phi_v$  values are obtained in the *S-10* flame, which indicates faster reactant mixing than in the *S-2* flame, as expected from fluid flow.

### Laminar Diffusion Flame (*S-2*)

Figure 4 shows the evolution of SiO<sub>2</sub> particle size and structure characteristics along the *S-2* laminar diffusion flame axis: (a) primary particle diameter  $d_{\text{v/s}}$  (triangles), geometric standard deviation  $\sigma_g$  (diamonds), and number density  $N$  (circles), and (b) aggregate radius of gyration  $R_g$  (hexagons), mass  $D_f$  (squares) and surface  $D_s$  fractal dimensions (stars), and primary particles per aggregate  $n_p$  (butterflies).

Early on when HAB < 1 cm, the formation of small particles is driven by chemical reaction (nucleation) and coagulation, which contribute to the increase in the primary particle diameter (from 6 to 9 nm) and to the broadening of the primary particle size distribution ( $\sigma_g$ , diamonds)<sup>[31]</sup> to a maximum of 1.6 at HAB = 1.8 cm as seen in premixed flames.<sup>[11,21]</sup> Further, the primary particle number density ( $N$ , circles) is initially constantly high, an indication of high particle formation rate balanced by coagulation losses early

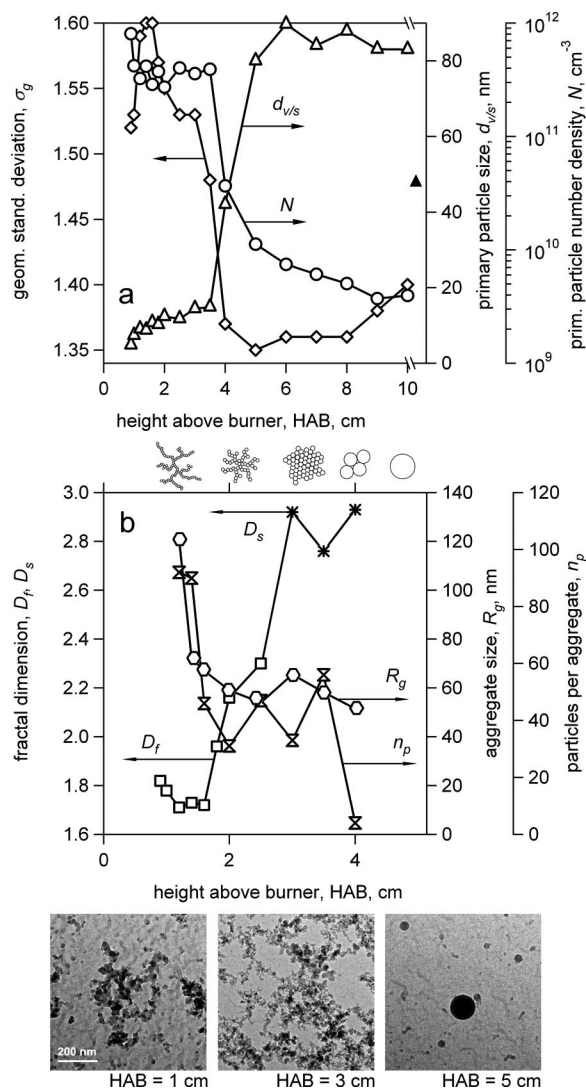


Figure 4. Evolution of the characteristics of the SiO<sub>2</sub> particles formed in the laminar diffusion flame *S-2*: (a) primary particle diameter ( $d_{\text{v/s}}$ , triangles), geometric standard deviation ( $\sigma_g$ , diamonds), and number density ( $N$ , circles); (b) mass ( $D_f$ , squares) or surface ( $D_s$ , stars) fractal dimension, aggregate radius of gyration ( $R_g$ , hexagons), and number of primary particles per aggregate ( $n_p$ , butterflies). TS-TEM images at three different HAB values (bottom) and a sketch of the particle structure evolution [on top of (b)] are shown. The  $d_{\text{v/s}}$  value of collected particles from the filter (filled triangle) is also given.

on. At roughly the same time (HAB < 2 cm), the value of  $D_f$  (Figure 4b, diamonds) is initially around 1.8 and slightly decreases to 1.7, which is consistent with cluster–cluster aggregation (CCA).<sup>[23,32]</sup>

Further downstream ( $1.8 < \text{HAB} < 3.5$  cm), the primary particle diameter ( $d_{\text{v/s}}$ , triangles) increases at a slower rate from 9 to 14 nm and its distribution ( $\sigma_g$ ) is narrowed as sintering starts to dominate, as smaller particles tend to sinter faster than bigger particles.<sup>[13]</sup> The aggregate size and the number of primary particles per aggregate decrease by sintering but reach plateaus of  $R_g = 60$  nm and  $n_p = 40$ , respectively, at about 3 cm. The  $D_f$  value, however, increases

from 1.7 to 2.9, which indicates compaction of the aggregates as they did not grow in size by coagulation as expected. In this region, the flame axis temperature reaches a plateau until the end of the (yellow) flame reaction zone at HAB = 4 cm (Figure 3, filled triangles). At these temperatures, aggregates become more compact by sintering and surface growth. At HAB = 3 cm, a fractal structure of these particles can no longer be assigned by conventional mass fractal analysis (Figure 2), therefore, only a surface fractal dimension can be ascribed to these structures (Figure 4b,  $D_s$ , stars).<sup>[28]</sup>

Above HAB = 3.5 cm, both  $R_g$  and especially  $n_p$  rapidly decrease (e.g. to  $n_p = 4$ ), while a  $D_f$  value close to 3 is obtained, which is indicative of compact particles or partially coalesced aggregates that form solid spheres (Figure 4). Further downstream, the particle morphology ( $D_f$  or  $D_s$ ,  $R_g$  and  $n_p$ ) can no longer be evaluated because of the limited  $q$  range. Simultaneously, the  $\sigma_g$  steeply drops to 1.37, a value below the self-preserving limit ( $\sigma_g = 1.45$ ). Here, approximately half of the silica is formed according to the evolution of  $\phi_v$  (Figure 3). The fast reduction in  $\sigma_g$  and the formation of the remaining particle mass (depicted by the final increase in  $\phi_v$ ) may result from surface growth on the particles that exhibited a steep increase in size to 90 nm ( $3.5 < \text{HAB} < 5$  cm) and are accompanied by a pronounced collapse in  $N$  and  $n_p$  as a result of sintering at these elevated temperatures. Surface growth can narrow the size distribution below the self-preserving limit (as shown for TiO<sub>2</sub>).<sup>[33]</sup> Further reduction in  $N$  and broadening of  $\sigma_g$  with increasing HAB arises because of coagulation and mixing with particle-laden gases from other streamlines.

On top of Figure 4b the evolution of particle size and morphology ( $d_{v/s}$ ,  $n_p$ ,  $R_g$ ,  $D_f$ ,  $D_s$ ) is sketched at the given HAB values. Moreover, below Figure 4b, TEM images of the particles thermophoretically collected at HAB = 1, 3 and 5 cm are shown. At HAB = 1 and 3 cm, fractal aggregates with small primary particles are observed, which collapse to form larger ones at HAB > 3 cm. This is in good agreement with SAXS measurements. At HAB = 1 cm, irregularly shaped, large particles are also seen, which most likely arise because of not fully oxidized HMDSO, which condenses on the TEM grid during thermophoretic sampling.<sup>[34]</sup> Early in the flame, not all HMDSO is fully oxidized to SiO<sub>2</sub>, as has been observed by FTIR spectroscopy.<sup>[12]</sup> The observed particle growth at HAB < 3.5 cm (Figure 4a, triangles) indicates that indeed the temperature in the center of the *S-2* flame should be lower than 2500 K (Figure 2, filled triangles),<sup>[29]</sup> because otherwise the small structures (Figure 4b insets) would have sintered quickly at these temperatures.<sup>[35]</sup>

At the end of the flame (HAB > 7.5 cm), the *in-situ* detected primary particle diameter (Figure 4a open triangles) is 83 nm in the centerline, whereas *ex-situ* USAXS measurements (Figure 4a, filled triangle, Table 1) of the final powder collected from the filter exhibits sizes of 48 nm that are consistent with N<sub>2</sub> adsorption (BET) and TEM analysis (Figure 1, Table 1).<sup>[36,37]</sup> The difference in particle size of *in-situ* (SAXS) and *ex-situ* measurements (USAXS,

BET, TEM) is attributed to the fact that particles on the filter come from different stream lines and have a broader particle size distribution, as seen in the TEM image in Figure 1.

### Turbulent Diffusion Flame (*S-10*)

In Figure 5 the evolution of the SiO<sub>2</sub> particle characteristics in the turbulent diffusion flame (*S-10*) are shown along the flame axis, as has been shown for the *S-2* flame. Early on, reactant mixing, reaction, and coagulation<sup>[31]</sup> result in rather small primary particles 10 nm in diameter ( $d_{v/s}$ , Figure 5a), having a broad primary particle size distribution ( $\sigma_g = 1.6$ , Figure 5a) at low HAB (< 0.8 cm). The five-times higher O<sub>2</sub> flow rate for the *S-10* flames diluted  $N$ , which results in about a five-times lower number concentration than that for the *S-2* flame. As a result of coagulation and sintering at the beginning, fractal aggregates with a  $D_f$  value of 2.1 (Figure 5b), an aggregate size of 95 nm (Figure 5b), and a large number of primary particles ( $n_p = 100$ , Figure 5b) are formed.

Further downstream (HAB > 0.8 cm) sintering tends to narrow  $\sigma_g$ , but short residence times limited sintering (in contrast to that observed for the *S-2* flame), which results in small  $d_{v/s}$  values and broad  $\sigma_g$  along the flame axis. The evolution of the mass fractal dimension ( $D_f$ , Figure 5b) at low HAB values shows a decrease to 1.75 at HAB = 1.5–2 cm, similar to that observed for the *S-2* flame (Figure 4b, squares), but at lower HAB values, higher  $D_f$  values (= 2.1) are detected. These  $D_f$  values correspond to cluster–cluster aggregation (CCA).<sup>[23,32]</sup> The evolution of both  $R_g$  and  $n_p$  in the turbulent flame was similar to that of the *S-2* flame but at lower HAB values. The  $R_g$  and  $n_p$  values decrease by sintering early on and reach a rather constant value towards the end of the flame with  $D_f = 2$ –2.1, which is consistent with CCA.

The primary particle number density,  $N$  (triangles), increases steadily up to HAB = 3 cm, which indicates that the formation of new particles by chemical reaction is detected close to the visual flame end (Table 1). Further downstream,  $N$  is reduced by dilution through air entrainment induced by turbulence.

In the early stages of this flame (HAB = 0.4 cm), large structures ( $\approx 200$  nm) are seen in the TEM inset of Figure 5. Similarly to the large particles seen in Figure 4, these particles arise from HMDSO that is not fully oxidized to SiO<sub>2</sub> early in the flame.<sup>[34]</sup> At HAB = 1 cm, smaller aggregates are formed relative to those at HAB = 0.4 cm, but with larger, irregular primary particles (> 30 nm) than depicted by SAXS. This is an indication of condensation and reaction of HMDSO on the collected particles, which leads to the fast growth of oxidized or partially oxidized particles, which might not represent the actual particle size and morphology as detected by SAXS in the gas phase. Moreover, at HAB = 2 cm, the primary particle diameter as well as the aggregate size are reduced as the chemical reaction is completed and the precursor (HMDSO) is consumed,

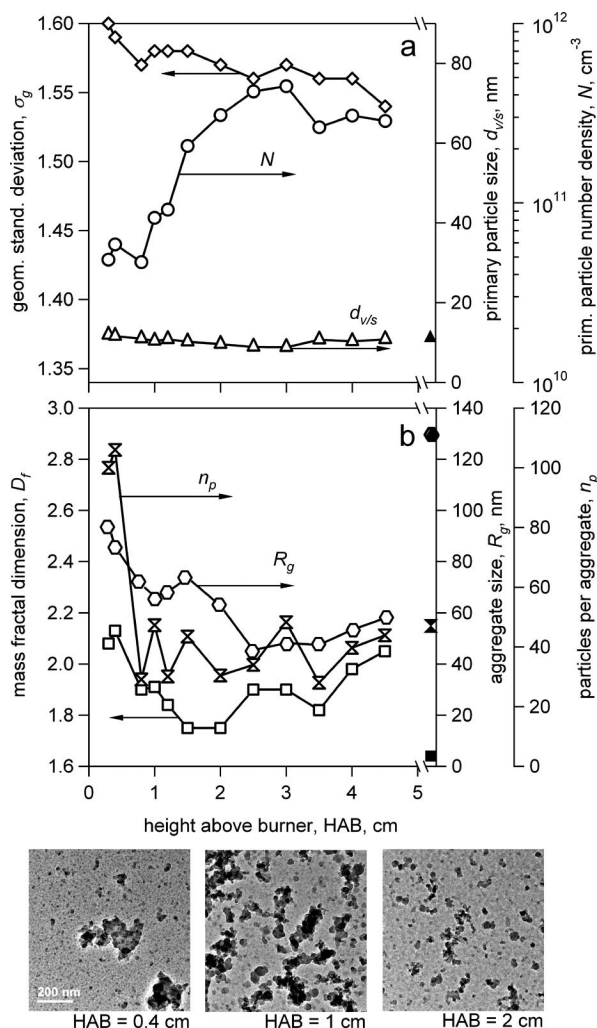


Figure 5. Evolution of the characteristics of the SiO<sub>2</sub> particles formed in the turbulent diffusion flame S-10: (a) primary particle diameter ( $d_{v/s}$ , triangles), geometric standard deviation ( $\sigma_g$ , diamonds), and number density ( $N$ , circles); (b) mass fractal dimension ( $D_f$ , squares), aggregate radius of gyration ( $R_g$ , hexagons), and number of primary particles per aggregate ( $n_p$ , butterflies). TEM images at three different HAB values are shown (bottom). The  $d_{v/s}$ ,  $D_f$ ,  $R_g$ , and  $n_p$  values of collected particles from the filter (filled symbols) are also given.

which diminishes its condensation effect on the thermophoretically collected particles.

*Ex-situ* USAXS measurements of the product powder (Figure 2a) reveals that the primary particle diameter ( $d_{v/s} = 11$  nm) is consistent with *in-situ* SAXS results. However, the  $D_f$  value of these particles (Figure 5b, filled squares) exhibits a lower mass fractal dimension (1.64, P2 in Figure 2a) than that measured *in-situ* ( $D_f = 2.05$  at HAB = 4.5 cm). Mass fractal dimensions of 1.6–1.9 have been reported for turbulent diffusion flame-made particles,<sup>[12]</sup> which are similar to those of a premixed flame (14 g/h,  $D_f = 2.0$ ).<sup>[21]</sup> Very similar  $n_p$  values, but larger  $R_g$  values are detected. These differences are attributed again to the mixing of different particle stream lines.

## Conclusions

Application of *in-situ* SAXS on diffusion flames shows its ability to monitor fractal-like particle growth and leads to a detailed understanding of the evolution of particle size and morphology in over-ventilated laminar and turbulent diffusion flames.

Non-aggregated nanoparticles with large primary particles ( $\approx 100$  nm) were made in a laminar diffusion flame. In the early stages of the flame, chemical reaction (nucleation), coagulation, and sintering dominated particle growth to form fractal-like, aggregated particles consisting of small primary particles. As these aggregates experienced higher temperatures downstream, fast compaction took place by sintering, followed by surface growth, and finally full coalescence to form spherical particles.

Introduction of turbulence to the diffusion flame with increased flow of O<sub>2</sub> affected the flame temperature profile. This effectively converted the flame into a premixed-like one with characteristic high temperatures at the beginning, which decreased rapidly with higher O<sub>2</sub> dilution and air entrainment. Short high-temperature particle residence times controlled the extent of nucleation and sintering of SiO<sub>2</sub> and coagulation, which resulted in fractal-like, aggregated nanoparticles with small primary particles.

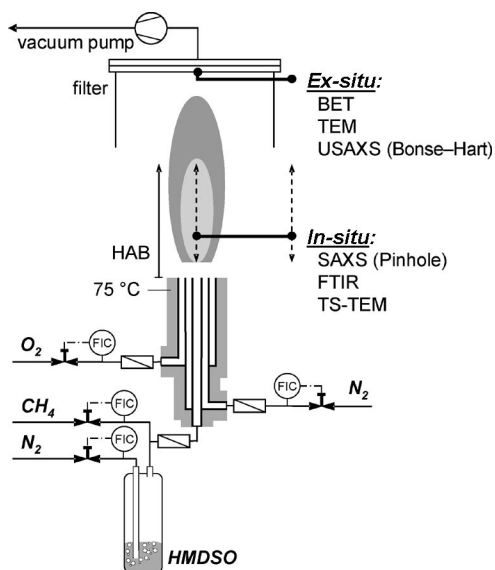
Early application of SAXS<sup>[23]</sup> allowed the distinction between aggregated and non-aggregated TiO<sub>2</sub> particles made in diffusion flames.<sup>[38]</sup> The SAXS work permitted the development and validation of detailed simulators interfacing particle dynamics with fluid mechanics in diffusion flames.<sup>[39,40]</sup> Further SAXS analysis has guided the development of models,<sup>[11]</sup> which distinguish between aggregates and agglomerates made by high-temperature aerosol processes. Such models and SAXS data<sup>[36,41,42]</sup> have guided the design of flame reactors for the synthesis (up to 20 g/h) of non-aggregated silica nanoparticles for acrylic dental nano composites and even the scaling up of these reactors for the manufacture of over 1 kg/h of nanostructured particles.<sup>[37]</sup> In turn, this work may allow for the more precise prediction of particle size and morphology in such diffusion reactors with varied geometries and large industrial units. It is expected that SAXS will be a valuable tool for reactor design and nanoparticle development in a wide variety of nano composite applications.

## Experimental Section

### Particle Synthesis

Scheme 1 shows the experimental setup for the synthesis of the SiO<sub>2</sub> nanoparticles with a co-flow diffusion flame, which has been presented in detail elsewhere.<sup>[43]</sup> Flow rates are given at standard temperature and pressure (STP). Hexamethyldisiloxane (HMDSO, Sigma Aldrich, purity > 98 %) vapor was delivered by bubbling 0.3 L/min of N<sub>2</sub> (PanGas, > 99.99 %) through a reservoir (flask volume: 1000 cm<sup>3</sup>). The concentration of HMDSO in that gas was controlled by the reservoir temperature (22 °C) by using a thermostated bath (Huber Kältemaschinenbau, Unistat CC, Offenburg, Germany), which resulted in an HMDSO consumption rate of

6.5 g/h or a SiO<sub>2</sub> production rate of 4.8 g/h. The HMDSO-laden N<sub>2</sub> gas flow was mixed with methane (0.5 L/min) and brought into the burner center tube. The first annulus was fed with N<sub>2</sub> (0.5 L/min), which prevented the formation of particles at the burner tip.<sup>[19]</sup> The second annulus was fed with O<sub>2</sub> (2–10 L/min, PanGas, >99.99 %). Constant gas flow rates were maintained by mass flow controllers (Bronkhorst, EL-Flow F201, Ruurlo, Netherlands). To prevent condensation of the precursor in the manifold, all tubes as well as the burner were heated to 75 °C with temperature-controlled heat hoses (Isopad, IHH105, Heidelberg, Germany) for gas delivery and glass silk heating tapes (Isopad, S45, Heidelberg, Germany) for the metal tubing.



Scheme 1. Experimental setup of the diffusion flame and measurement methods.

Product particles were collected on a glass fiber filter (Whatman Springfield Mill, GF/A, Maidstone, Kent, UK) placed in a stainless steel filter holder 30 cm above the visual flame tip (Scheme 1). Gas flow through the filter was maintained by the aid of a vacuum pump (Vacubrand RZ16, Wertheim, Germany). Set flame conditions are listed in Table 1 as  $S-y-y$  is the flow rate of oxygen (L/min).

Flame temperature profiles along the burner axis were obtained by recording emission/transmission spectra<sup>[24,44]</sup> by using a FTIR spectrometer (Bomem, MB155S, Quebec, Canada). The normalized radiance was compared to a best fit using the blackbody Planck function.<sup>[45,46]</sup> FTIR is a line-of-sight technique over the total flame width. The luminous flame zone was used to determine the visual flame height (Table 1).

### Particle Characterization

The specific surface area ( $SSA$ , m<sup>2</sup>/g) was determined by N<sub>2</sub> (PanGas, >99.999 %) adsorption according to the Brunauer–Emmett–Teller (BET) method at 77 K (Micromeritics, Tristar 3000, Belgium). The samples were outgassed (N<sub>2</sub>) at 150 °C for 1 h prior to analysis. The BET equivalent particle diameter ( $d_{\text{BET}}$ ) was calculated as  $d_{\text{BET}} = 6/(SSA \times \rho_{\text{particle}})$  by using the density of SiO<sub>2</sub> equal to 2.2 g/cm<sup>3</sup>.

For monitoring of particle growth along the flame axis at several heights above the burner, *in-situ* small-angle X-ray scattering (SAXS) at the European Synchrotron Radiation Facility (high brilliance beam line ID02, pinhole SAXS camera, ESRF Grenoble,

France)<sup>[47,48]</sup> was used. Monochromatic X-rays ( $\lambda = 1 \text{ \AA}$ ) with a beam cross-sectional area of  $200 \times 200 \text{ \mu m}$  penetrated the flame and were collected on the SAXS detector inside the 12-m long detector tube.<sup>[48]</sup> Two flame-to-detector distances (5 and 10 m) were used to cover a scattering wave vector  $q$  range ( $0.001 < q < 0.05 \text{ \AA}^{-1}$ ), whereas the scattering vector is defined as  $q = 4\pi \sin(\theta/2)/\lambda$  and  $\theta$  is the scattering angle.<sup>[41]</sup> The scattering curves of both configurations were combined prior to analysis. The exposure time of the charged-coupled-device camera was 0.3 s, and the collected scattering images were corrected as described elsewhere.<sup>[49]</sup> Background subtraction was carried out by using pure CH<sub>4</sub>/O<sub>2</sub> flames in the absence of HMDSO (no particle formation). The methane flow rate was increased (0.1 L/min) to obtain the same combustion enthalpies as that for the HMDSO-fed flames ( $B-y$ ; Table 1). Particle/aggregate characteristics were determined by *in-situ* SAXS data analysis following the unified fit model:<sup>[41,42]</sup> aggregate radius of gyration ( $R_g$ ), mass and surface fractal dimension ( $D_f$ ,  $D_s$ ), primary particle diameter ( $d_{v/s}$ ), geometric standard deviation ( $\sigma_g$ ), and number of primary particles per aggregate ( $n_p$ ). The silica volume fraction ( $\phi_v$ ) and the particle number density ( $N$ ) were also extracted. The primary particle diameter ( $d_{v/s}$ ) is obtained by the moment ratio, volume-to-surface,<sup>[36,37]</sup> as measured by BET analysis.

Collected particles were analyzed by *ex-situ* ultra small-angle X-ray scattering (USAXS in beam line ID02, Bonse–Hart camera, ESRF Grenoble, France).<sup>[50]</sup> A wider size range of 1  $\mu\text{m}$  to 1 nm was obtained with the USAXS setup than that for the SAXS configuration (100 to 1 nm, pinhole camera). However, with the Bonse–Hart USAXS camera longer measurement times in the order of 5–10 min were needed than for the fast *in-situ* SAXS measurements (20 ms). A small amount of as-prepared powder collected from the filter was placed between two adhesive tapes (Scotch, Magic, 3 M, France). Particle-free adhesive tapes were used for background subtraction. The USAXS setup allows detection of a broader  $q$  range especially at lower  $q$  ( $10^{-4} < q < 0.03 \text{ \AA}^{-1}$ ).

Thermophoretic sampling<sup>[51]</sup> (TS) was used to deposit particles onto carbon-coated copper TEM grids (Ted Pella Inc., USA) at different heights above the burner to assess particle morphology. The residence time of the TEM grids in the flame was approximately 50 ms, with an additional 50 ms for insertion and retraction. Subsequent (TEM) analysis was performed on a CM30 microscope (FEI; LaB<sub>6</sub> cathode, operated at 300 kV). TEM images were recorded on a slow-scan CCD camera.

### Acknowledgments

We thank Dr. F. Krumeich at EMEZ (ETH Zurich) for TEM imaging and the Swiss National Science Foundation (SNF 200021-114095) and Commission of Technology and Innovation (CTI-7949.3) for financial support.

- [1] S. E. Pratsinis, S. V. R. Mastrangelo, *Chem. Eng. Prog.* **1989**, 85, 62–66.
- [2] K. Wegner, S. E. Pratsinis, *Chem. Eng. Sci.* **2003**, 58, 4581–4589.
- [3] G. D. Ulrich, *Chem. Eng. News* **1984**, 62, 22–29.
- [4] S. E. Pratsinis, *Prog. Energ. Combust.* **1998**, 24, 197–219.
- [5] M. S. Wooldridge, *Prog. Energ. Combust.* **1998**, 24, 63–87.
- [6] H. K. Kammler, L. Madler, S. E. Pratsinis, *Chem. Eng. Technol.* **2001**, 24, 583–596.
- [7] P. Roth, *Proc. Comb. Inst.* **2007**, 31, 1773–1788.
- [8] P. D. Christofides, M. H. Li, L. Madler, *Powder Technol.* **2007**, 175, 1–7.

- [9] R. Strobel, A. Baiker, S. E. Pratsinis, *Adv. Powder Technol.* **2006**, *17*, 457–480.
- [10] R. Strobel, S. E. Pratsinis, *J. Mater. Chem.* **2007**, *17*, 4743–4756.
- [11] S. Tsantilis, H. K. Kammler, S. E. Pratsinis, *Chem. Eng. Sci.* **2002**, *57*, 2139–2156.
- [12] R. Mueller, H. K. Kammler, S. E. Pratsinis, A. Vital, G. Beaucage, P. Burtscher, *Powder Technol.* **2004**, *140*, 40–48.
- [13] M. C. Heine, S. E. Pratsinis, *J. Aerosol Sci.* **2007**, *38*, 17–38.
- [14] L. Madler, W. J. Stark, S. E. Pratsinis, *J. Appl. Phys.* **2002**, *92*, 6537–6540.
- [15] R. Strobel, M. Maciejewski, S. E. Pratsinis, A. Baiker, *Thermochim. Acta* **2006**, *445*, 23–26.
- [16] E. J. Mezey in *Vapor Deposition* (Eds.: C. F. Powell, J. H. Oxley, J. M. Blocher), Wiley, New York, **1966**, pp. 423.
- [17] P. B. Zantye, A. Kumar, A. K. Sikder, *Mater. Sci. Eng. R* **2004**, *45*, 89–220.
- [18] G. P. Fotou, S. Vemury, S. E. Pratsinis, *Chem. Eng. Sci.* **1994**, *49*, 4939–4948.
- [19] H. K. Kammler, R. Mueller, O. Senn, S. E. Pratsinis, *AIChE J.* **2001**, *47*, 1533–1543.
- [20] A. Vital, J. Richter, R. Figi, O. Nagel, C. G. Aneziris, J. Bernardi, T. Graule, *Ind. Eng. Chem. Res.* **2007**, *46*, 4273–4281.
- [21] H. K. Kammler, G. Beaucage, D. J. Kohls, N. Agashe, J. Ilavsky, *J. Appl. Phys.* **2005**, *97*, 054309.
- [22] G. Beaucage, H. K. Kammler, R. Mueller, R. Strobel, N. Agashe, S. E. Pratsinis, T. Narayanan, *Nat. Mater.* **2004**, *3*, 370–374.
- [23] J. Hyeon-Lee, G. Beaucage, S. E. Pratsinis, S. Vemury, *Langmuir* **1998**, *14*, 5751–5756.
- [24] H. K. Kammler, S. E. Pratsinis, P. W. Morrison, B. Hemmerling, *Combust. Flame* **2002**, *128*, 369–381.
- [25] W. H. Zhu, S. E. Pratsinis, *AIChE J.* **1997**, *43*, 2657–2664.
- [26] A. Guinier, G. Fournet in *Small-Angle Scattering of X-rays*, Wiley, New York, **1955**.
- [27] G. Porod in *Small-Angle X-ray Scattering* (Eds: O. Glatter, O. Kratky), Academic Press, London, **1982**.
- [28] A. J. Hurd, D. W. Schaefer, J. E. Martin, *Phys. Rev. A* **1987**, *35*, 2361–2364.
- [29] R. J. Santoro, T. T. Yeh, J. J. Horvath, H. G. Semerjian, *Combust. Sci. Technol.* **1987**, *53*, 89–115.
- [30] G. D. Ulrich, *Combust. Sci. Technol.* **1971**, *4*, 47.
- [31] J. D. Landgrebe, S. E. Pratsinis, *Ind. Eng. Chem. Res.* **1989**, *28*, 1474–1481.
- [32] D. W. Schaefer, A. J. Hurd, *Aerosol Sci. Technol.* **1990**, *12*, 876–890.
- [33] S. Tsantilis, S. E. Pratsinis, *Langmuir* **2004**, *20*, 5933–5939.
- [34] K. Nakaso, K. Okuyama, M. Shimada, S. E. Pratsinis, *Chem. Eng. Sci.* **2003**, *58*, 3327–3335.
- [35] S. Tsantilis, H. Briesen, S. E. Pratsinis, *Aerosol Sci. Technol.* **2001**, *34*, 237–246.
- [36] G. Beaucage, H. K. Kammler, S. E. Pratsinis, *J. Appl. Crystallogr.* **2004**, *37*, 523–535.
- [37] H. K. Kammler, G. Beaucage, R. Mueller, S. E. Pratsinis, *Langmuir* **2004**, *20*, 1915–1921.
- [38] S. E. Pratsinis, W. H. Zhu, S. Vemury, *Powder Technol.* **1996**, *86*, 87–93.
- [39] T. Johannessen, S. E. Pratsinis, H. Livbjerg, *Chem. Eng. Sci.* **2000**, *55*, 177–191.
- [40] T. Johannessen, S. E. Pratsinis, H. Livbjerg, *Powder Technol.* **2001**, *118*, 242–250.
- [41] G. Beaucage, *J. Appl. Crystallogr.* **1995**, *28*, 717–728.
- [42] G. Beaucage, *Phys. Rev. E* **2004**, *70*, 031401
- [43] A. Teleki, S. E. Pratsinis, K. Wegner, R. Jossen, F. Krumeich, *J. Mater. Res.* **2005**, *20*, 1336–1347.
- [44] P. E. Best, R. M. Carangelo, J. R. Markham, P. R. Solomon, *Combust. Flame* **1986**, *66*, 47–66.
- [45] P. R. Griffiths, J. A. Haseth in *Fourier Transform Infrared Spectroscopy*, Wiley, New York, **1986**. P.
- [46] W. Morrison, R. Raghavan, A. J. Timpone, C. P. Artelt, S. E. Pratsinis, *Chem. Mater.* **1997**, *9*, 2702–2708.
- [47] T. Narayanan, O. Diat, P. Bosecke, *Nucl. Instrum. Meth. A* **2001**, *467*, 1005–1009.
- [48] M. Sztucki, T. Narayanan, G. Beaucage, *J. Appl. Phys.* **2007**, *101*, 114304.
- [49] D. Pontoni, T. Narayanan, J. M. Petit, G. Grubel, D. Beysens, *Phys. Rev. Lett.* **2003**, *90*, 188301.
- [50] M. Sztucki, T. Narayanan, *J. Appl. Crystal.* **2007**, *40*, 459–462.
- [51] R. A. Dobbins, C. M. Megaridis, *Langmuir* **1987**, *3*, 254–259.

Received: October 5, 2007

Published Online: January 25, 2008